

Supporting Information

Mesoporous Mo-doped PtBi intermetallic metallene superstructures to enable the complete electrooxidation of ethylene glycol

Xiaotong Yang,^a Qiang Yuan,^{*a} Tian Sheng^{*c} and Xun Wang^{*b}

^a State-Local Joint Laboratory for Comprehensive Utilization of Biomass, Center for R&D of Fine Chemicals, College of Chemistry and Chemical Engineering, Guizhou University, Guiyang, Guizhou Province 550025, P. R. of China

^b Key Lab of Organic Optoelectronics & Molecular Engineering, Tsinghua University, Beijing 100084, P. R. of China

^c College of Chemistry and Materials Science, Anhui Normal University, Wuhu 241000, P. R. of China

*Corresponding author.

E-mails: qyuan@gzu.edu.cn; wangxun@mail.tsinghua.edu.cn; TSheng@ahnu.edu.cn

Experimental section

Chemicals:

Platinum (II) acetylacetonate ($\text{Pt}(\text{acac})_2$, 98%) was purchased from CIVI-CHEM. Bismuth (III) nitrate pentahydrate ($\text{Bi}(\text{NO}_3)_3 \cdot 5\text{H}_2\text{O}$, 99.0%) and Potassium hydroxide (KOH, 95%) were purchased from Macklin. Polyvinylpyrrolidone (PVP-K30) was purchased from Sigma-Aldrich. Ammonium bromide (NH_4Br , 99%) was purchased from Aladdin. Molybdenum carbonyl ($\text{Mo}(\text{CO})_6$, 98%) and Pt black were obtained from Alfa Aesar. Pt/C (60 wt%) catalyst was obtained from Johnson Matthey. N, N-dimethylformamide (DMF, 99.5%), ethylene glycol (EG, AR), ethanol (AR) and isopropanol (AR) were purchased from Sinopharm Chemical Reagent Co. Ltd. (Shanghai, China). Chemicals were used as received without further purification.

Synthesis of M-PtBiMo IMSs

For this synthesis, $\text{Pt}(\text{acac})_2$ (12 mg), $\text{Bi}(\text{NO}_3)_3 \cdot 5\text{H}_2\text{O}$ (10 mg), $\text{Mo}(\text{CO})_6$ (20 mg), PVP-K30 (100 mg) and NH_4Br (80 mg) were dispersed in DMF (8 mL) by stirring. After stirring for 30 min, the mixture was transferred to an autoclave (12 mL) and heated from room temperature to 150 °C and held at 150 °C for 8 h. The products were collected by centrifugation and washed with ethanol solution several times.

Synthesis of PtBi NPs

The PtBi NPs were synthesized under the same procedure for synthesis of M-PtBiMo IMSs at the absence of $\text{Mo}(\text{CO})_6$.

Characterizations

The morphology was analyzed by TEM (JEM-1400 Flash) and high-resolution high-angle annular dark-field scanning transmission electron microscopy (HAADF-STEM) (FEI, Themis Z). The X-ray diffraction (XRD) patterns of the samples were recorded on a Bruker D8 Advance diffractometer with Cu $K\alpha$ radiation ($\lambda=1.5418 \text{ \AA}$) with graphite monochromator (40 KV, 40 mA). X-ray photoelectron spectroscopy (XPS) was conducted on a Thermo Scientific™ K-Alpha™+ spectrometer equipped with a monochromatic Al $K\alpha$ X-ray source (1486.6 eV) operating at 100 W. Binding energy was corrected from charge effects by reference to the C1s peak of carbon at 284.8 eV. The inductively coupled plasma optical emission spectrometry (ICP-OES) analysis of samples was performed on iCAP 7200 (ThermoFisher) and determined the compositions.

Electrochemical measurements

All electrochemical measurements for the EGOR test were performed at room temperature by employing a three-electrode electrochemical cell with an electrochemical workstation (CHI,

760E). The glassy carbon electrode (GC, $\Phi=5$ mm) was employed as the working electrode, along with the carbon rod as the counter electrode and the Ag/AgCl electrode as the reference electrode. The loading mass of the precious metal (Pt metal) recorded by performing ICP-OES on the GC electrodes containing M-PtBiMo IMSs, PtBi NPs, Pt/C, and Pt black was 1.57 μg , 1.54 μg , 1.77 μg and 1.5 μg , respectively. The cyclic voltammograms (CVs) were recorded in the N_2 -saturated 1 M KOH solution or 1 M KOH +1 M EG solution from -0.8 to 0.2 V (vs. Ag/AgCl) at a rate of 50 mV s^{-1} . Later, the current-time ($I-t$) test was performed at -0.25 V for 10000 s. The electrochemical impedance spectra (EIS) were recorded in the frequency range from 100 kHz to 0.01 Hz with an amplitude of 5 mV at -0.25 V in the mixture composed of 1 M KOH and 1 M EG.

CO-Stripping measurements

All samples were carried out firstly in the N_2 -saturated 0.1 M HClO_4 solution to test from -0.25 to 0.9 V (vs. Ag/AgCl) at a scan rate of 50 mV s^{-1} , then inlet CO until saturation and recorded the CVs.

***In situ* anti-CO performance**

The *in situ* anti-CO poisoning experiments were carried out in 1 M KOH + 1 M EG solution. Before performing CVs, CO gas was first inputted with a flow rate of 5 mL min^{-1} for 15 min, then kept CO inputting and CV scanning was performed.

Electrochemical *in situ* FTIR spectra measurements

The measurement of electrochemical *in situ* Fourier transform infrared (*in situ* FTIR) reflection spectroscopy was conducted on a Nicolet-iS50 FT-IR spectrometer containing a liquid-nitrogen-cooled MCT-A detector, at a spectral resolution of 8 cm^{-1} . The species (absorbed and dissolved) were measured on a thin layer (<10 μm) toward the working electrode and CaF_2 window for *in situ* FTIR. Multi-stepped FTIR spectroscopy (MS-FTIR) was utilized to collect spectra in 1 M KOH +1 M EG electrolytes from -0.9 to 0.2 V (vs. Ag/AgCl) at 0.1 V intervals. The relative change in reflectivity ($\Delta R/R$) of spectra was calculated by the following equation:

$$\Delta R/R = (R(E_S) - R(E_R)) / R(E_R)$$

Where $R(E_S)$ and $R(E_R)$ are single-beam spectra collected at the sample potential E_S and reference potential E_R .

Membrane electrode assembly fabrication and fuel cell performance test

The anode catalyst inks were made by mixing the M-PtBiMo IMSs, XC-72, ultrapure water, isopropyl alcohol, and 5% Nafion solution. After sonication for 1 h, the ink was dripped on the foam nickel (1.44 cm^2) for the anode catalyst layer. The load capacity of the metal is 60%. Meanwhile, 4.8 mg Pt/C and 20 μL of Nafion solution (5 wt%) were dispersed in a mixture

solution of 800 μL isopropanol and 200 μL ultrapure water and then dripped onto the gas diffusion layer (AvCard GDS2240, 1.44 cm^2) to gain the cathode catalyst. The precious metal (Pt) loading of the anode and cathode is 1 mg cm^{-2} and 2 mg cm^{-2} , respectively. For comparison, commercial Pt/C (60%, JM) prepared anode and cathode catalysts under the same conditions. An anion-exchange membrane, Fumasep FAAM-20 (FuMa-Tech) was soaked in 6 M KOH for 24 h to convert it to an OH^- environment, before being rinsed and stored in ultrapure water. Then, the cathode catalyst layer, anion-exchange membrane, and anode catalyst layer were sandwiched using hot-pressing at 70 $^\circ\text{C}$ and 1 MPa for 100 s. After that, a Fuel Cell Test System (850e, Scribner Associates Inc.) was used to obtain polarization and power density curves to determine the polarization performance of actual DEGFCs. Wherein, the mixture solution (3 mL min^{-1}) of 6 M KOH with 1 M EG was pumped to anode, and oxygen (300 mL min^{-1}) was fully humidified and supplied to cathode without bank pressure simultaneously while maintaining the cell temperature at 80 $^\circ\text{C}$. After holding the cell for half an hour under the above conditions, the stable polarization and power density curves were gained by using a galvanostatic polarization mode. The durability tests were performed at 400 mA cm^{-2} for 10 h at 80 $^\circ\text{C}$.

Computational methods

Electronic structure calculations were performed using the QE package with the generalized gradient approximation (GGA) of Perdew-Burke-Ernzerhof (PBE) to the exchange-correlation functional.¹⁻³ The electronic-ion interactions were considered in the form of the projector-augmented-wave (PAW) method. The kinetic cutoff energy for a plane-wave function was 35 Ry. The five-layer p (1×1) PtBi (110) surface was modeled by 20 Pt and 20 Bi atoms, and one surface Pt atom was replaced by one Bi atom to model the PtBiMo intermetallic, as shown in Fig. S17[†]. The bottom three layers were fixed and other atoms were relaxed during all optimizations. For the calculation of theoretical O adsorption potential, we use the free energy of $\frac{1}{2} \text{H}_2$ in the gas phase to replace that of $\text{H}^+ + \text{e}^-$, due to the equilibrium of $\text{H}^+ + \text{e}^- \rightarrow \frac{1}{2} \text{H}_2$ at the standard electrode condition.⁴ All vibrational frequencies of adsorbates were calculated based on the harmonic oscillators approximation.⁵ According to the experimental pH value, the calculated potentials at the standard hydrogen electrode condition are converted into the potential referred to as the Ag/AgCl electrode. The adsorption energy in this work was defined as $E_{\text{ad}} = E(\text{ad/int}) - E(\text{ad}) - E(\text{surf})$, where $E(\text{ad/int})$, $E(\text{ad})$, and $E(\text{int})$ are the total energies of the adsorbate binding to the surface, free adsorbate in vacuum and clean surface, respectively. The reaction energy, $\text{AH}^* \rightarrow \text{A}^* + \text{H}^*$, was calculated as $\Delta E = E(\text{A}^*) + E(\text{H}^*) - E(\text{AH}^*) - E(\text{surf})$.

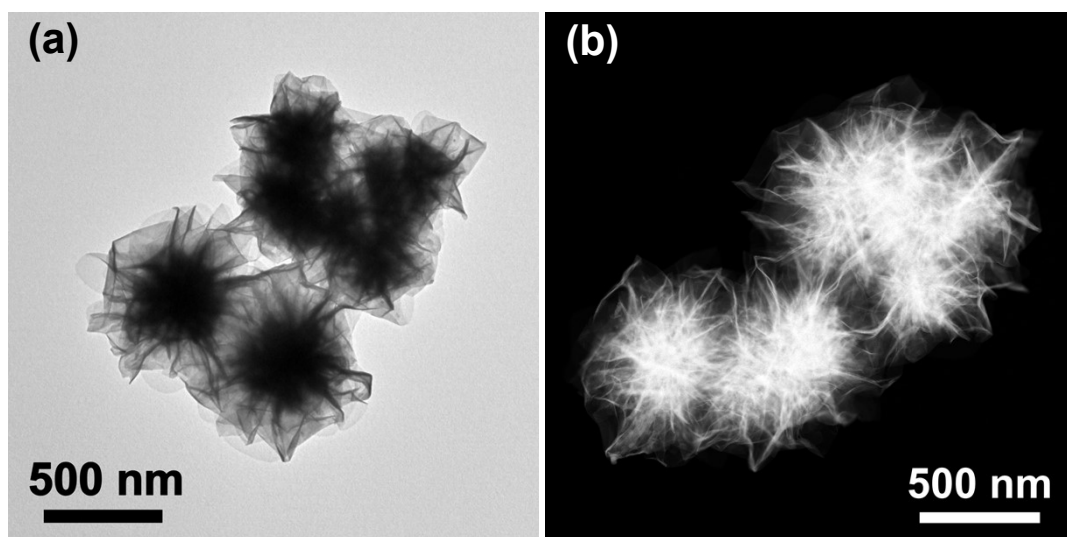


Fig. S1 (a) TEM and (b) HAADF-STEM images of the M-PtBiMo IMSs.

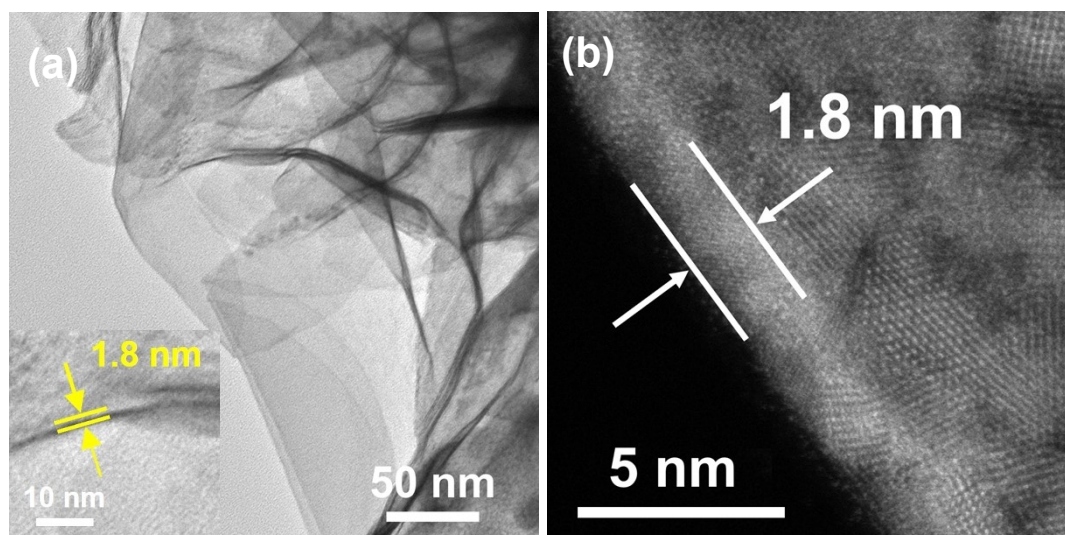


Fig. S2 (a) TEM and (b) HAADF-STEM images of the M-PtBiMo IMSs.

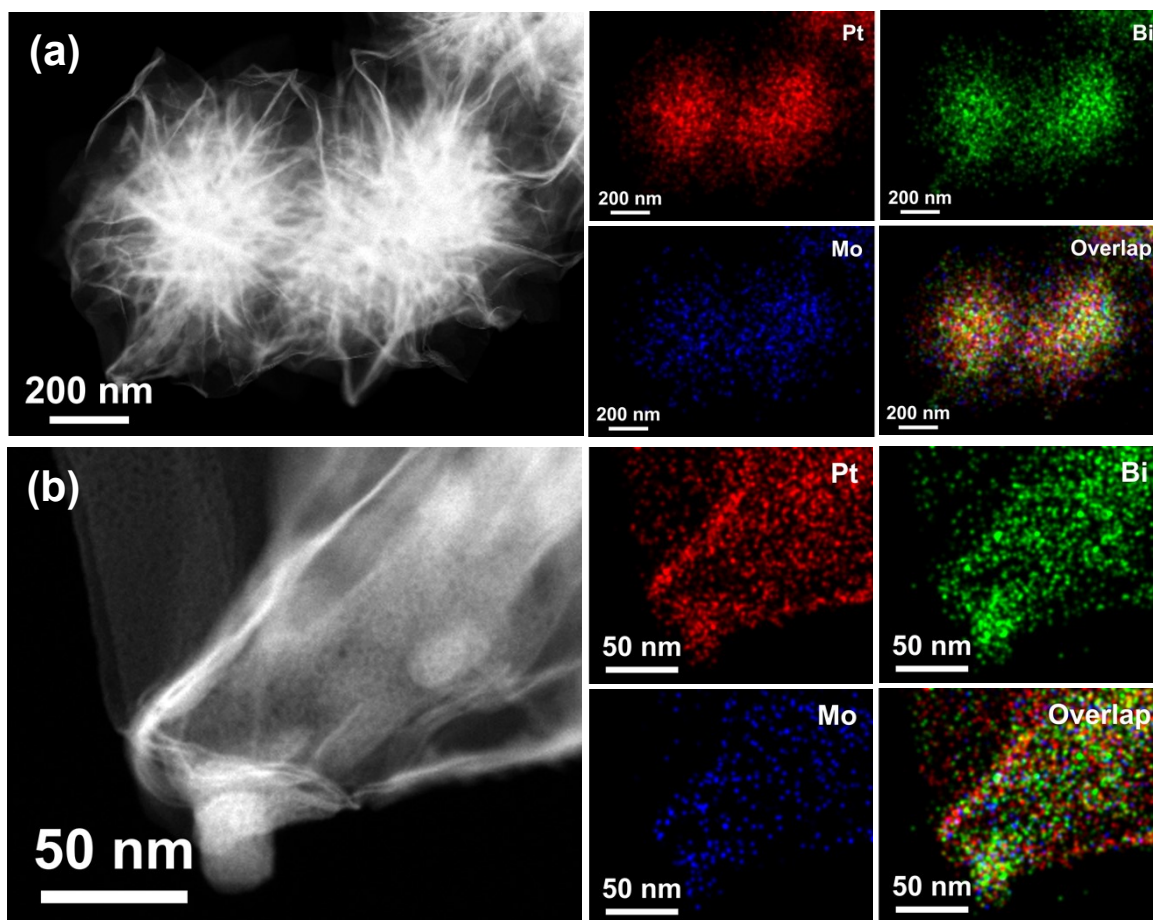


Fig. S3 (a, b) HAADF-STEM images and corresponding elemental mappings of M-PtBiMo IMSs at different positions and magnifications.

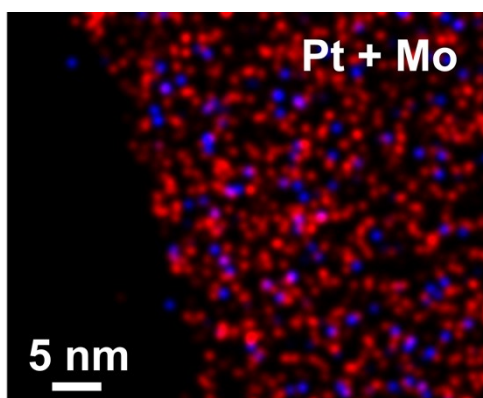


Fig. S4 The elemental mapping of Pt and Mo.

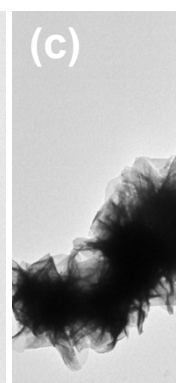
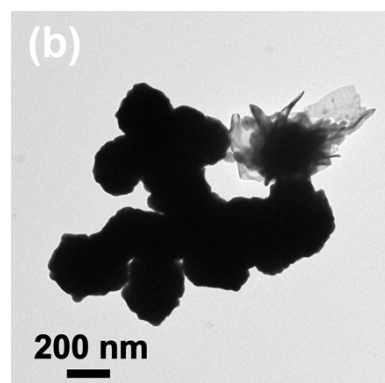
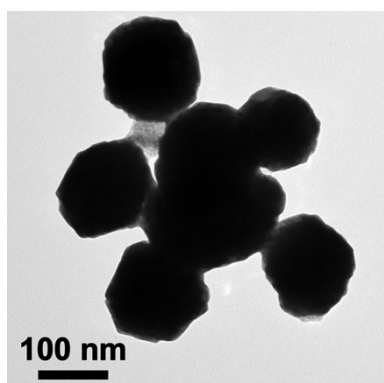


Fig. S5 TEM images of the products synthesized with the same reaction conditions as those of M-PtBiMo IMSs except the use of (a) 0 mg, (b) 10 mg, (c) 40 mg $\text{Mo}(\text{CO})_6$.

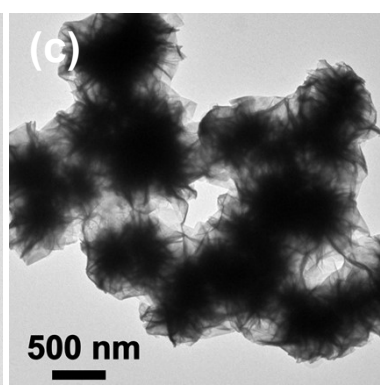
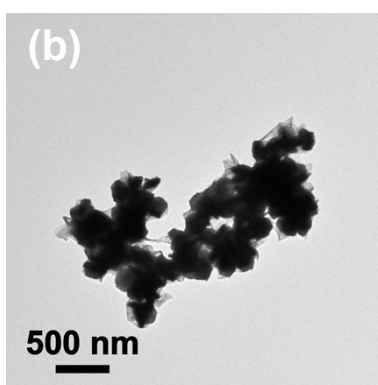
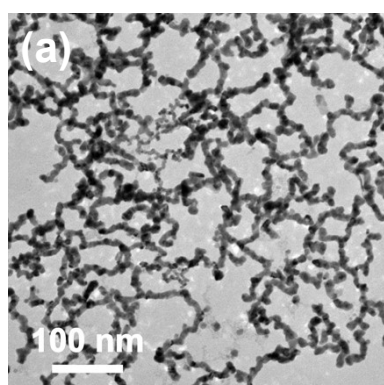


Fig. S6 TEM images of the products synthesized with the same reaction conditions as those of M-PtBiMo IMSs except the use of (a) 0 mg, (b) 40 mg, and (c) 120 mg NH_4Br .

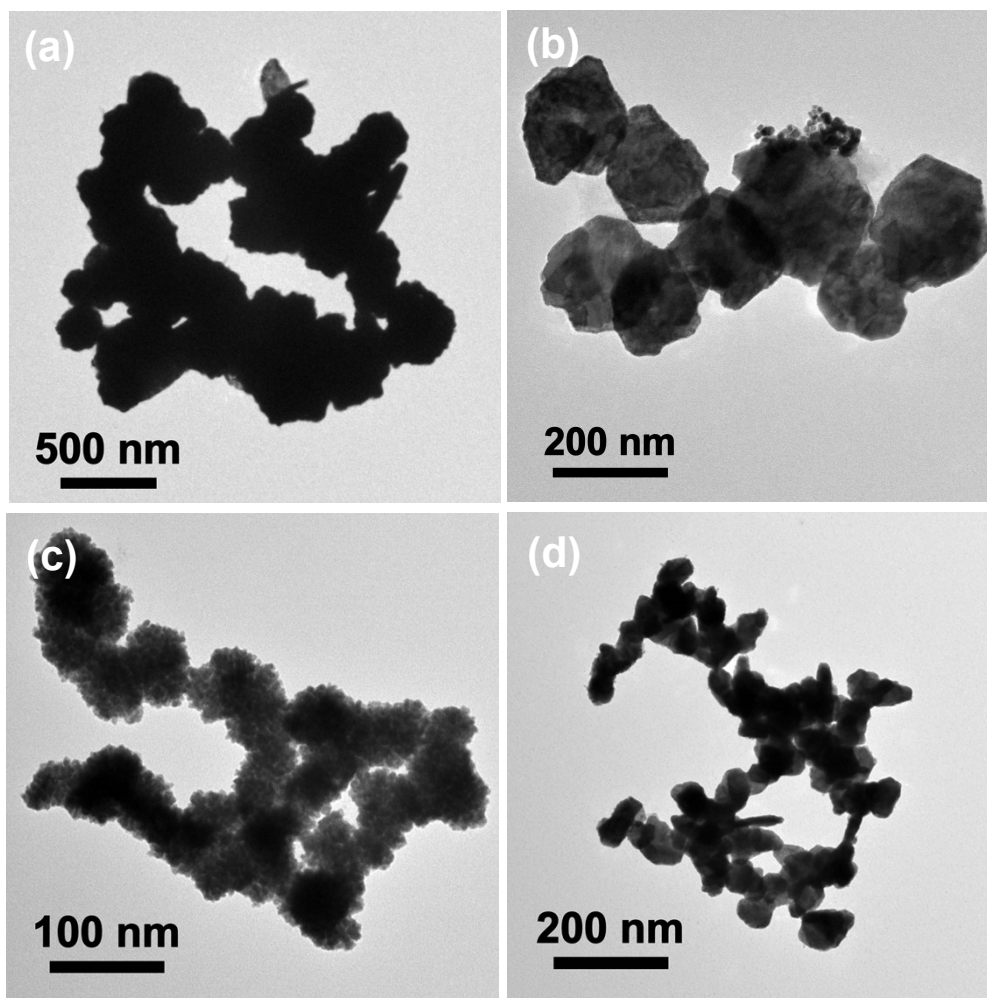


Fig. S7 TEM images of the products synthesized with the same reaction conditions as those of M-PtBiMo IMSs except for the replacement of $Mo(CO)_6$ with an equal mole of (a) $W(CO)_6$, (b) $Cr(CO)_6$, (c) $Ru(CO)_{12}$, and (d) $Co_2(CO)_8$.

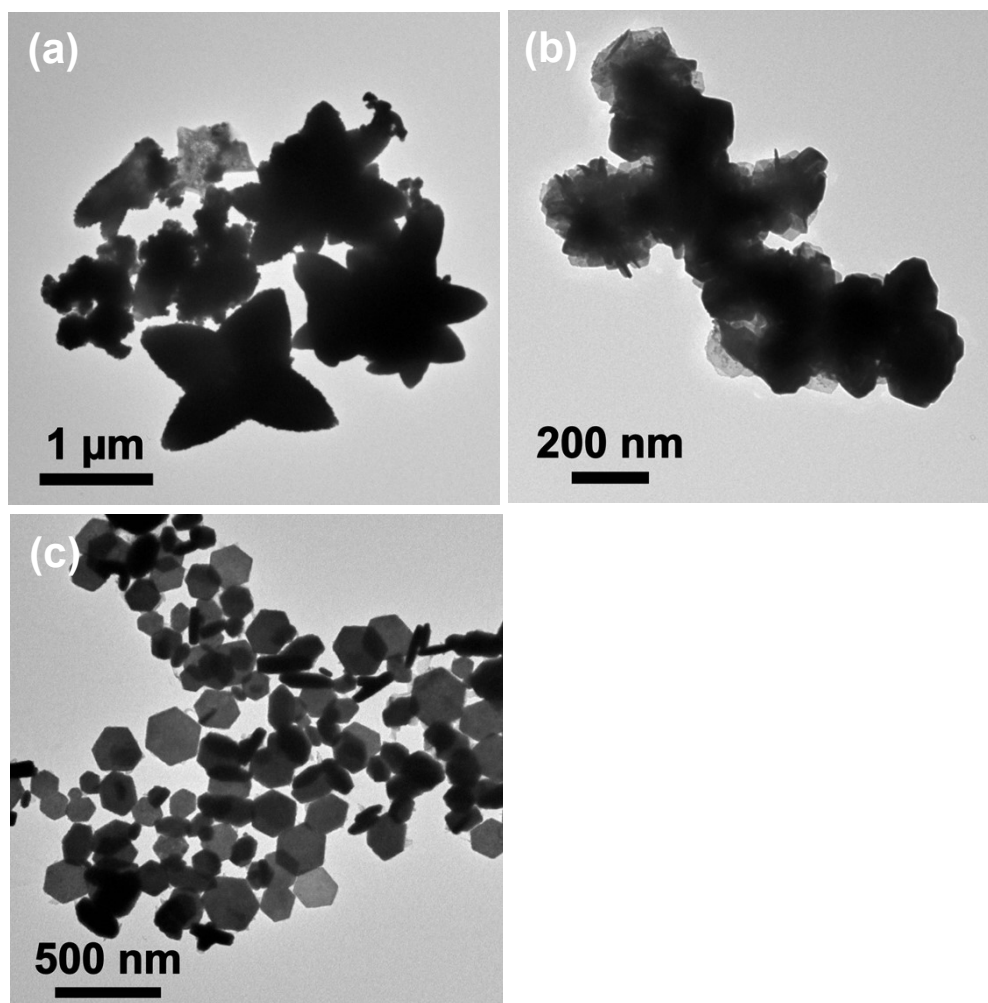


Fig. S8 TEM images of the products synthesized with the same reaction conditions as those of M-PtBiMo IMSs except for the replacement of NH_4Br with an equal mole of (a) NH_4F , (b) NH_4Cl and (c) NH_4I .

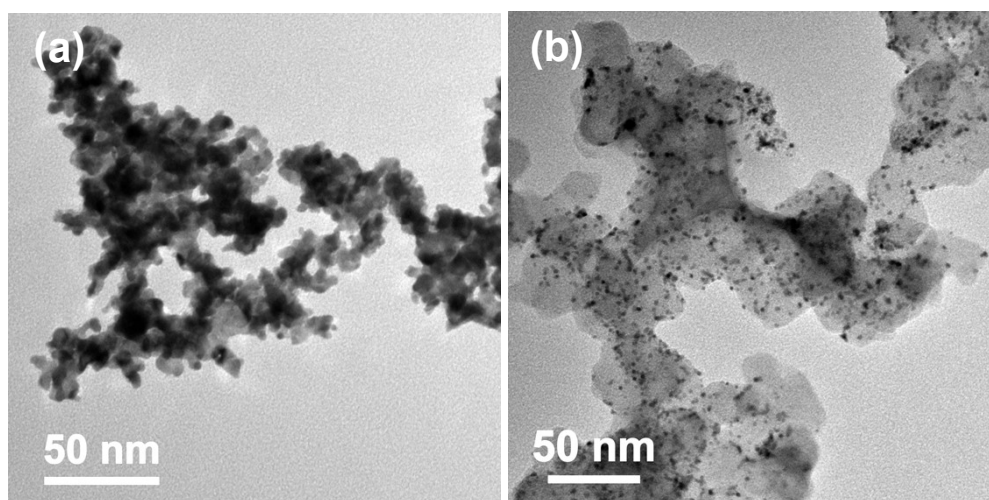


Fig. S9 The TEM images of Pt black (a) and Pt/C (b).

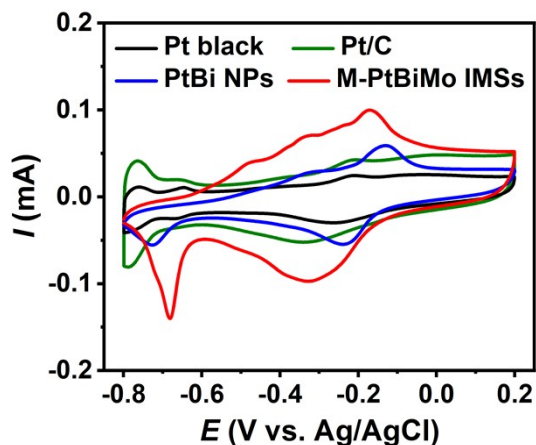


Fig. S10 CV curves of M-PtBiMo IMSs, PtBi NPs, Pt/C and Pt black in N_2 -saturated 1 M KOH at 50 mV s^{-1} .

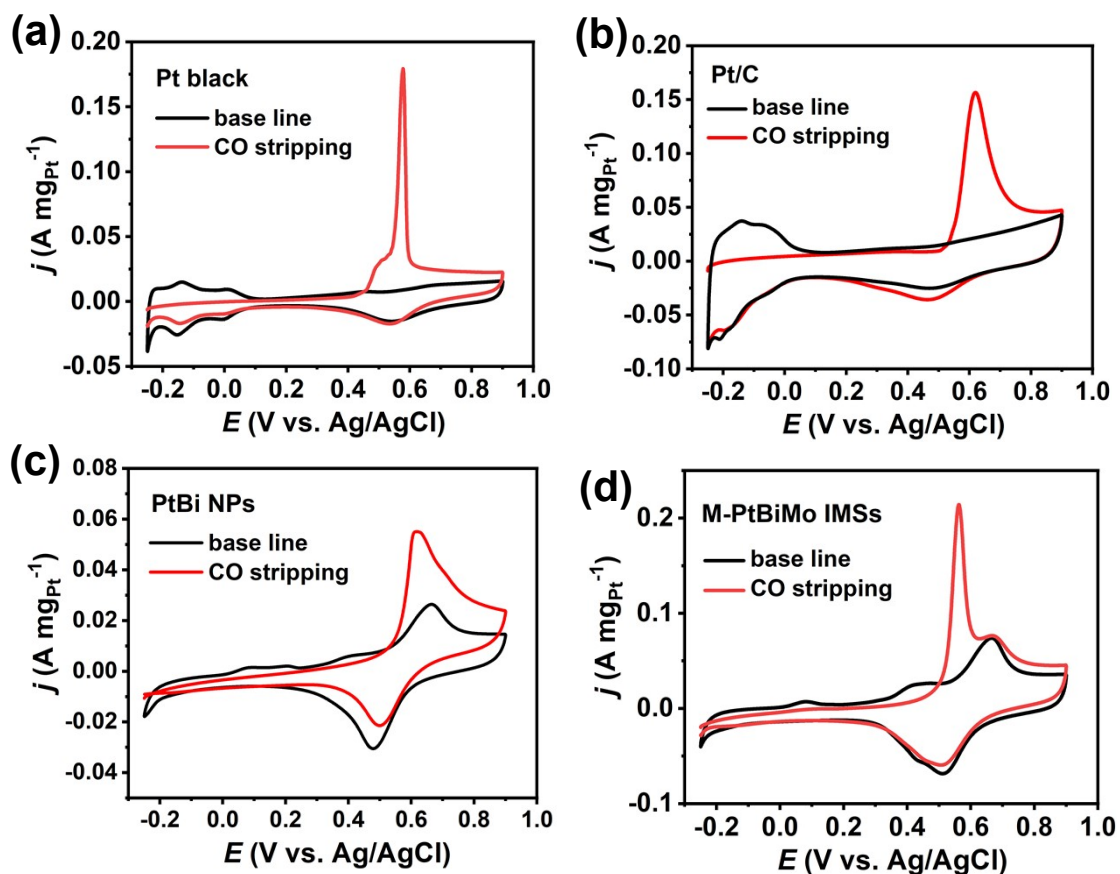


Fig. S11 CO stripping measurements of (a) Pt black, (b) Pt/C, (c) PtBi NPs, and (d) M-PtBiMo IMSs catalysts in 0.1 M HClO_4 solution at a scan rate of 50 mV s^{-1} . (Red line is the CO stripping and the black line is base line.)

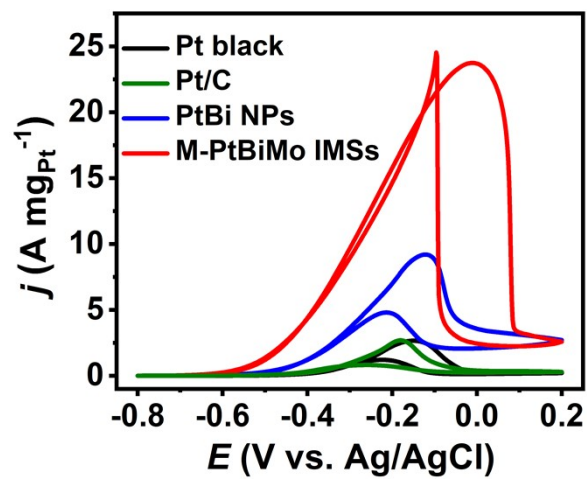


Fig. S12 CV curves after the $I-t$ test.

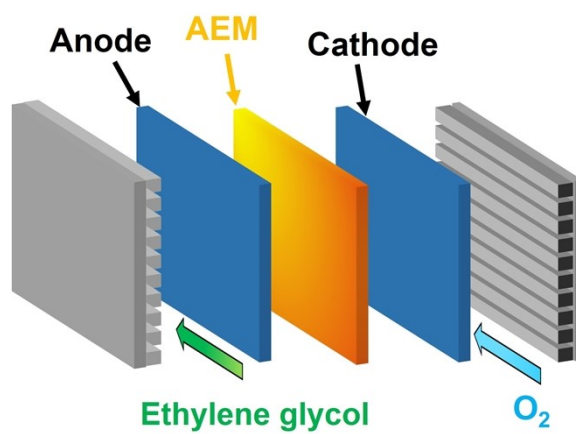


Fig. S13 The schematic diagram for the assembled DEGFC device.

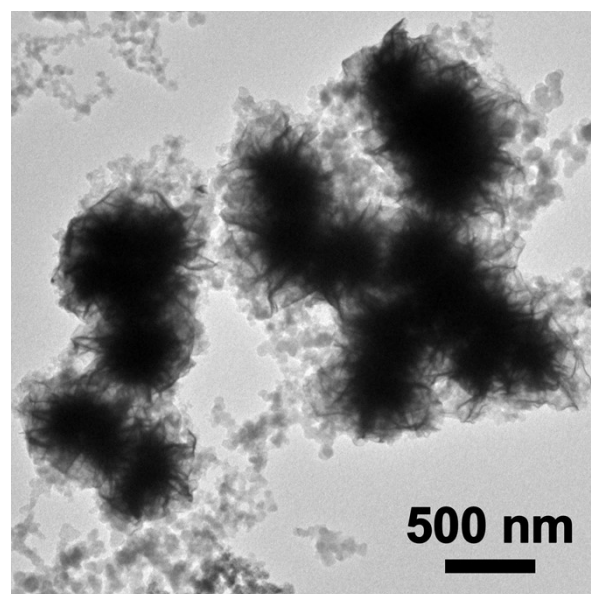


Fig. S14 TEM image of M-PtBiMo IMSs after durability test.

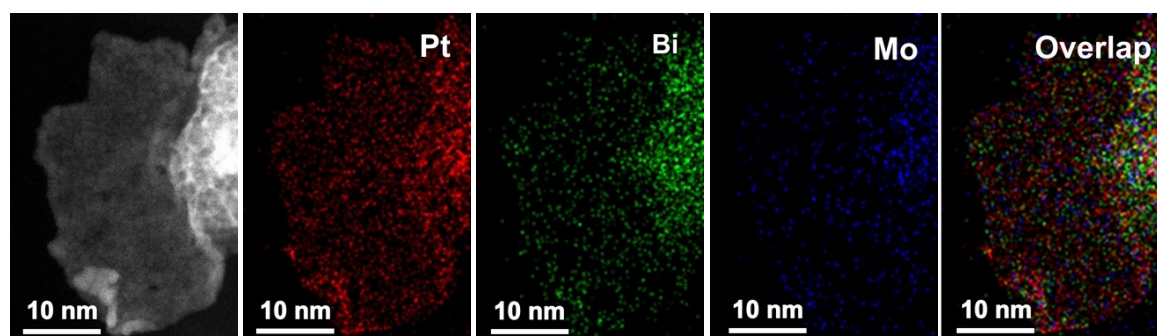


Fig. S15 HAADF-STEM image and corresponding elemental mappings of M-PtBiMo IMSs after 10 h durability testing in DEGFC.

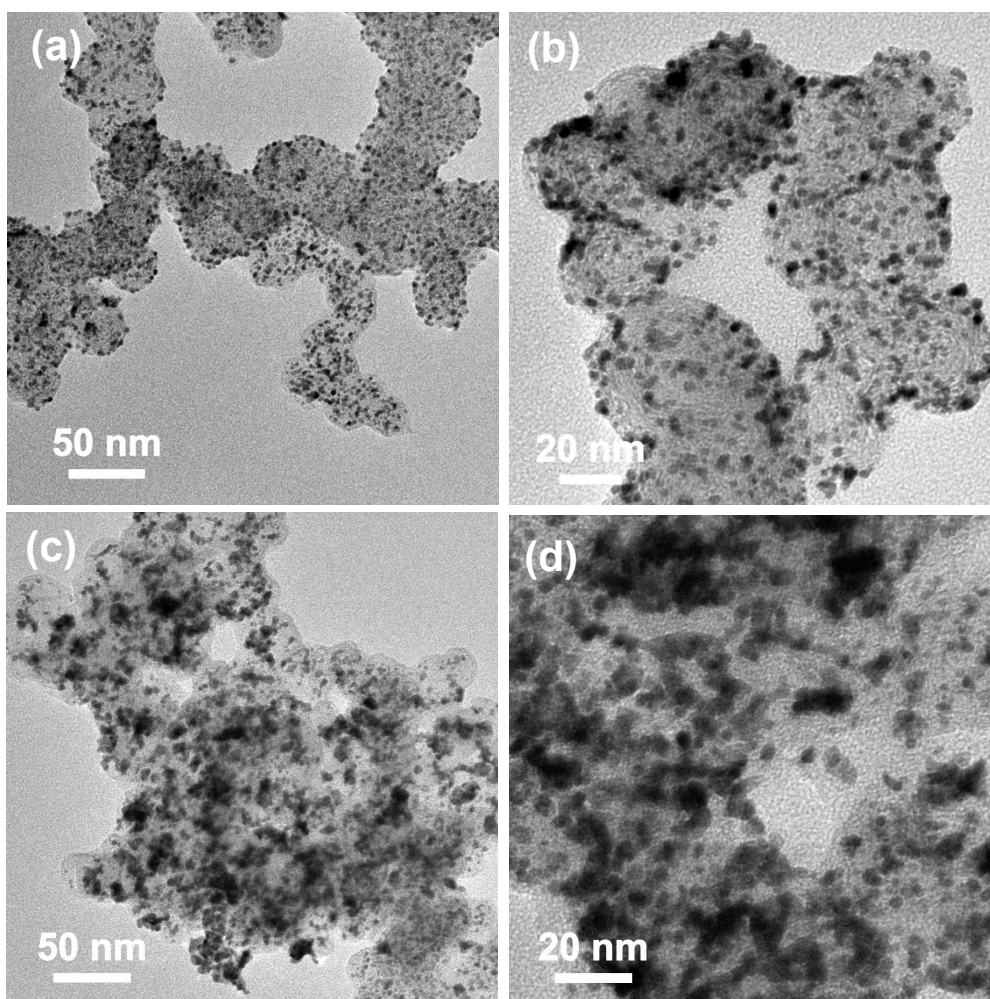


Fig. S16. TEM images of Pt/C (a, b) before and (c, d) after the durability test.

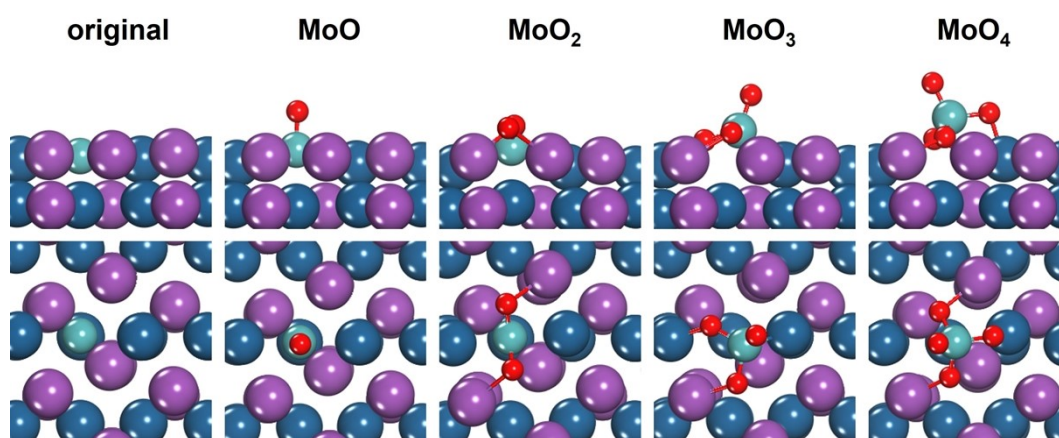


Fig. S17 Side and top views of the PtBiMo surface with different amounts of O atoms. Blue: Pt; purple: Bi; green: Mo; red: O.

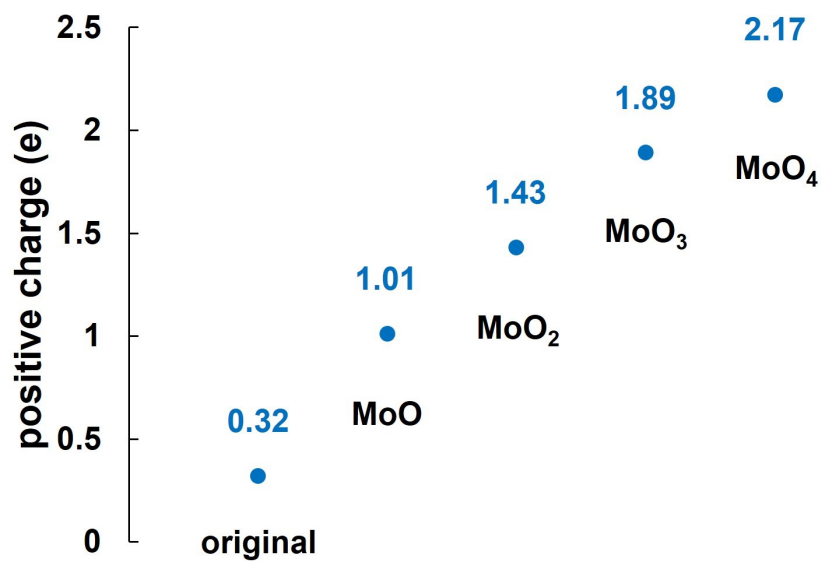


Fig. S18 Bader charge in the Mo atom with different amounts of O atoms.

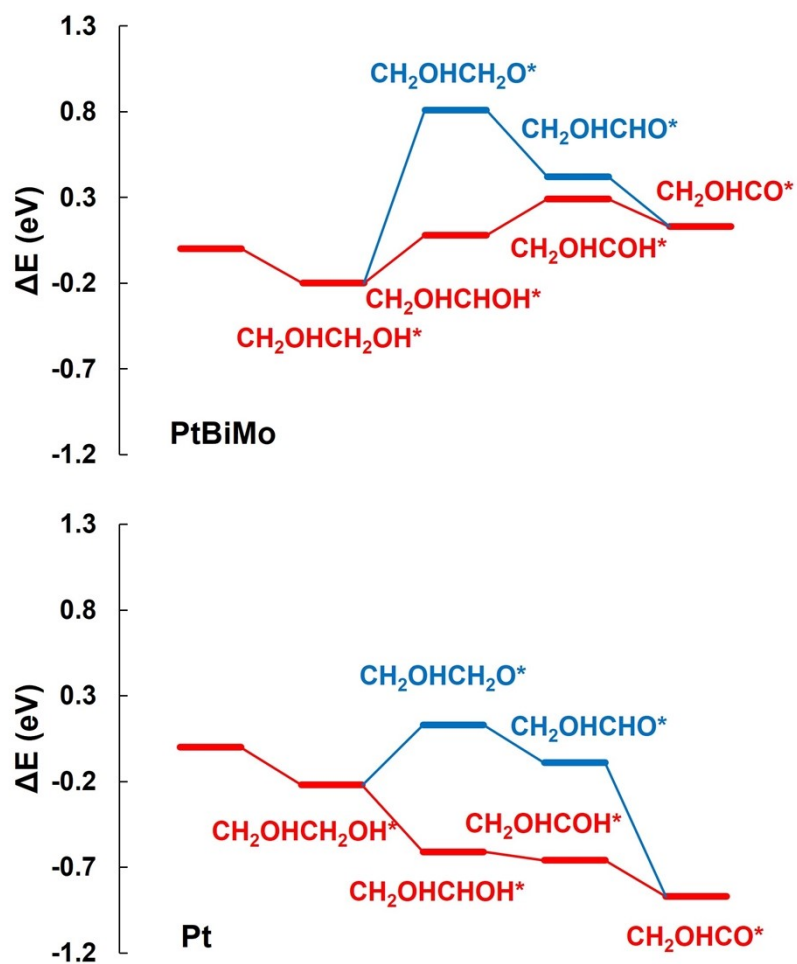


Fig. S19 Energy profiles for the dehydrogenation of EG on PtBiMo and Pt respectively.

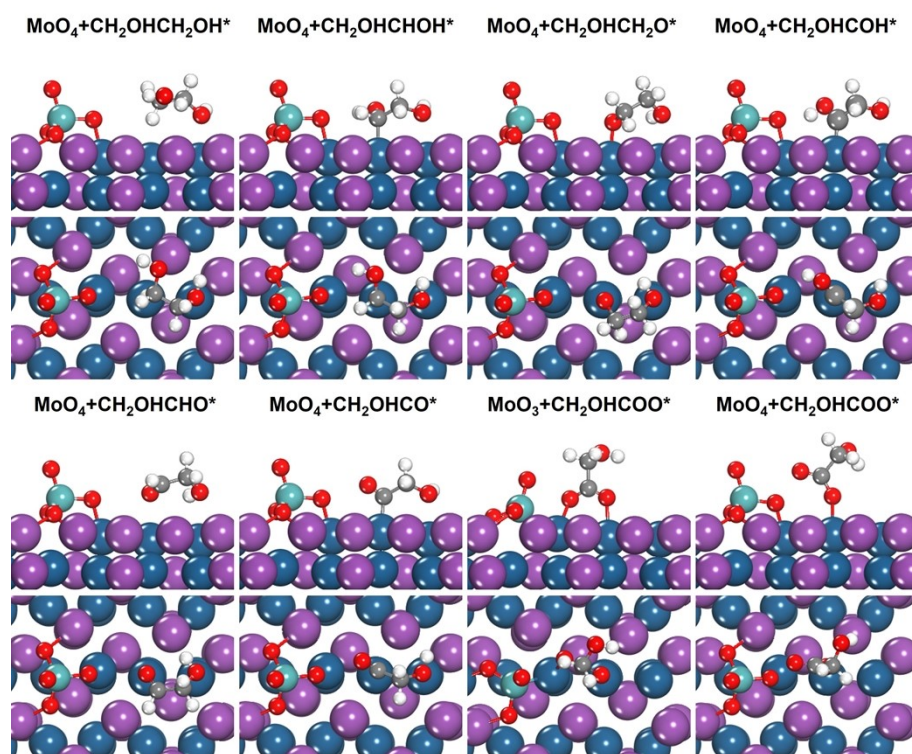


Fig. S20 Side and top views of intermediates in the EG electrooxidation to glycolate on PtBiMo.

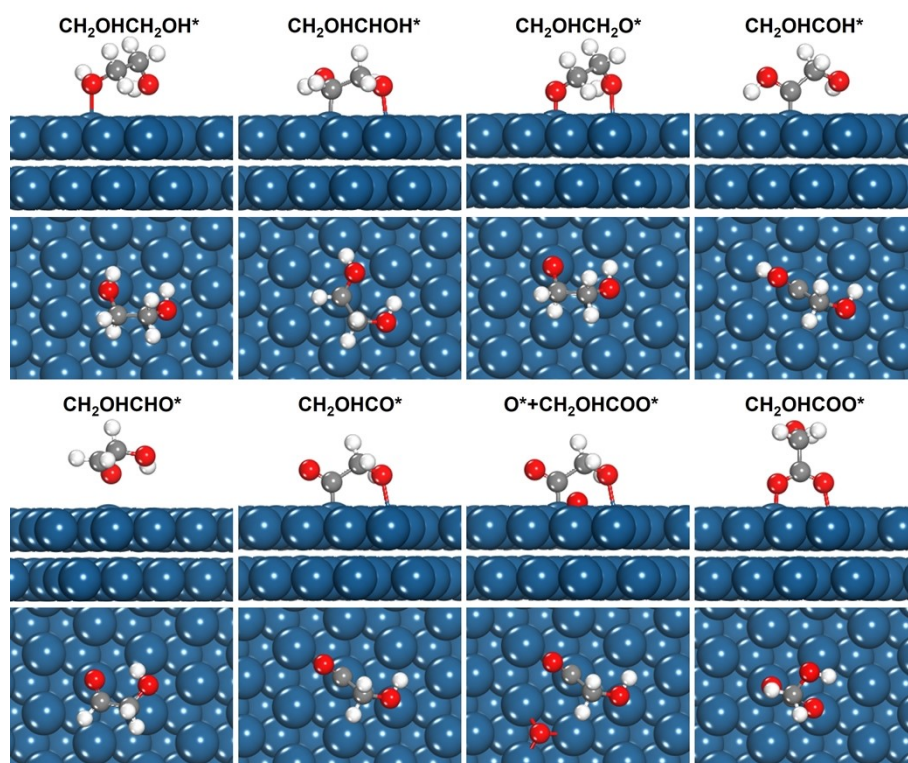


Fig. S21 Side and top views of intermediates in the EG electrooxidation to glycolate on Pt.

Table S1. A comparison of the EGOR catalytic mass activities and specific activities of the typical Pd, Pt-based catalysts was reported in the literature.

| Catalysts | Electrolyte | Mass activity (A mg ⁻¹) | Specific activity (mA cm ⁻²) | Reference |
|--|-----------------------|--|---|-----------|
| M-PtBiMo IMSs | 1 M KOH + 1 M EG | 24.0 | 61.1 | This work |
| PtNi NRs | 1 M KOH + 1 M EG | 7.26 | 18.1 | 6 |
| Pd ₃ Pb NCs | 1 M KOH + 1 M EG | 4.06 | 16.8 | 7 |
| Pt/Rh metallene | 1 M KOH + 3 M EG | 4.25 | 8.39 | 8 |
| Pd-WO _{2.75} | 1 M KOH + 1 M EG | 4.58 | 4.97 | 9 |
| PtRh-S NC | 1 M KOH + 1 M EG | 5.13 | 11.6 | 10 |
| Pd-PdSe HNSs | 1 M KOH + 1 M EG | 8.6 | 15.7 | 11 |
| Pd ₇ Ag NSs | 0.5 M KOH + 1 M EG | 7.01 | 14.1 | 12 |
| Pd/a-MnO ₂ | 1 M KOH + 0.5 M EG | 10.5 | 24.7 | 13 |
| PdCu nanosheets | 1 M KOH + 1 M EG | 4.71 | 13.7 | 14 |
| Pt _{4.5} Pb NWs | 0.5 M NaOH + 0.5 M EG | 13.5 | 5.7 | 15 |
| PtBi NFs | 1 M KOH + 1 M EG | 5.29 | - | 16 |
| Au@PdPt | 1 M KOH + 1 M EG | 3.02 | - | 17 |
| PtPbBi HNPs | 1 M NaOH + 1 M EG | 10.22 | - | 18 |
| Pt ₃₂ Pd ₄₈ Ni ₂₀ NSs | 0.5 M KOH + 0.5 M EG | 9.77 | - | 19 |
| Ptc/Ti ₃ C ₂ Tx | 1 M KOH + 1 M EG | 15.1 | - | 20 |

Table S2. DEGFCs performance comparison of M-PtBiMo IMSs and many reported catalysts.

| Anode catalyst | Cathode catalyst | Test conditions | Peak power density | References |
|--|------------------------|------------------------------|---------------------------|------------|
| M-PtBiMo IMSs | Pt/C | 6M KOH + 1M EG at 80 °C | 173.6 mW cm ⁻² | This work |
| 3D Pt _{53.1} Bi _{43.4} Au _{3.5} | Pt/C | 6 M KOH + 3M EG at 80 °C | 145 mW cm ⁻² | 21 |
| D-PdPtCu/C | D-PdPtCu/C | 6 M KOH + 1M EG at 75 °C | 137 mW cm ⁻² | 22 |
| Pd-(Ni-Zn)/C | Fe-Co/C | 2 M KOH + 5 wt% EG at 80 °C | 95 mW cm ⁻² | 23 |
| Pt/C | Fe-Cu-N4/C (Acta 4020) | 2 M KOH + 1 M EG at 50 °C | 71.0 mW cm ⁻² | 24 |
| Pd ₅₂ -Ni ₄₈ /NSCNT | Pt/C | 1 M KOH + 0.5 M EG at 25 °C | 62.8 mW cm ⁻² | 25 |
| Pd/TNTAweb | Fe-Co/C | 2 M KOH + 10 wt% EG at 25 °C | 45 mW cm ⁻² | 26 |
| PtPdAuCuFe/C | Pt/C | 6 M KOH + 2 M EG at 80 °C | 17.63 mW cm ⁻² | 27 |
| P-(PtCo ₄ @Pt)/C | Pt/C | 1 M KOH + 2 M EG at 60 °C | 14.48 mW cm ⁻² | 28 |
| PtPdAuNiCo/C | Pt/C | 6 M KOH + 2 M EG at 80 °C | 8.38 mW cm ⁻² | 29 |
| PtRu/C | Pt/C | 1 M KOH + 5 M EG at 50 °C | 7.4 mW cm ⁻² | 30 |

References

- (1) P. Giannozzi, S. Baroni, N. Bonini, M. Calandra, R. Car, C. Cavazzoni, D. Ceresoli, G. L. Chiarotti, M. Cococcioni, I. Dabo, A. Dal Corso, S. de Gironcoli, S. Fabris, G. Fratesi, R. Gebauer, U. Gerstmann, C. Gougoussis, A. Kokalj, M. Lazzeri, L. Martin-Samos, N. Marzari, F. Mauri, R. Mazzarello, S. Paolini, A. Pasquarello, L. Paulatto, C. Sbraccia, S. Scandolo, G. Sclauzero, A. P. Seitsonen, A. Smogunov, P. Umari and R. M. Wentzcovitch, *J. Phys.: condens. Matter*, 2009, **21**, 395502.
- (2) J. P. Perdew, K. Burke and M. Ernzerhof, *Phys. Rev. Lett.*, 1996, **77**, 3865-3868.
- (3) D. Vanderbilt, *Phys. Rev. B Condens. Matter*, **1990**, *41*, 7892-7895.
- (4) J. K. Norskov, J. Rossmeisl, A. Logadottir, L. Lindqvist, J. R. Kitchin, T. Bligaard and H. Jonsson, *J. Phys. Chem. B*, 2004, **108**, 17886-17892.

- (5) A. A. Gokhale, S. Kandoi, J. P. Greeley, M. Mavrikakis and J. A. Dumesic, *Chem. Eng. Sci.*, 2004, **59**, 4679-4691.
- (6) Y. P. Zhang, F. Gao, P. P. Song, J. Wang, T. X. Song, C. Wang, C. Y. Chen, L. J. Jin, L. Li, X. Zhu and Y. K. Du, *J. Power Sources*, 2019, **425**, 179-185.
- (7) H. Xu, P. Song, C. Fernandez, J. Wang, M. Zhu, Y. Shiraishi and Y. Du, *ACS Appl. Mater. Interfaces*, 2018, **10**, 12659-12665.
- (8) H. Wang, Y. Liang, S. Liu, H. Yu, K. Deng, Y. Xu, X. Li, Z. Wang and L. Wang, *Inorg. Chem.*, 2023, **62**, 14477-14483.
- (9) L. Karuppasamy, C. Y. Chen, S. Anandan and J. J. Wu, *ACS Appl. Mater. Interfaces*, 2019, **11**, 10028-10041.
- (10) F. Gao, Y. P. Zhang, P. P. Song, J. Wang, T. X. Song, C. Wang, L. Song, Y. Shiraishi and Y. K. Du, *J. Mater. Chem. A*, 2019, **7**, 7891-7896.
- (11) Y. Qin, W. Zhang, F. Wang, J. Li, J. Ye, X. Sheng, C. Li, X. Liang, P. Liu, X. Wang, X. Zheng, Y. Ren, C. Xu and Z. Zhang, *Angew. Chem., Int. Ed.* 2022, **61**, e202200899.
- (12) F. Gao, Y. Zhang, F. Ren, Y. Shiraishi and Y. Du, *Adv. Funct. Mater.*, 2020, **30**, 2000255.
- (13) Y. Wang, J. L. Liu, H. J. Yuan, F. Liu, T. J. Hu and B. Q. Yang, *Adv. Funct. Mater.*, 2023, **33**, 2211909.
- (14) X. Z. Guo, H. Y. Shang, J. Guo, H. Xu and Y. K. Du, *Appl. Surf. Sci.*, 2019, **481**, 1532-1537.
- (15) Y. Feng, L. Bu, S. Guo, J. Guo and X. Huang, *Small*, 2016, **12**, 4464-4470.
- (16) Y. P. Zhang, F. Gao, P. P. Song, J. Wang, T. X. Song, C. Wang, C. Q. Wang, J. Guo and Y. K. Du, *J. Alloys. Compd.*, 2019, **789**, 834-840.
- (17) X. Yang, Q. Wang, S. Qing, Z. Gao, X. Tong and N. Yang, *Adv. Energy Mater.*, 2021, **11**, 2100812.
- (18) Z. Zhu, F. Liu, J. Fan, Q. Li, Y. Min and Q. Xu, *ACS Appl. Mater. Interfaces*, 2020, **12**, 52731-52740.
- (19) J. Lai, F. Lin, Y. Tang, P. Zhou, Y. Chao, Y. Zhang and S. Guo, *Adv. Energy Mater.*, 2019, **9**, 1800684.
- (20) J. Zhu, L. Xia, R. Yu, R. Lu, J. Li, R. He, Y. Wu, W. Zhang, X. Hong, W. Chen, Y. Zhao, L. Zhou, L. Mai and Z. Wang, *J. Am. Chem. Soc.*, 2022, **144**, 15529-15538.
- (21) X. T. Yang, K. X. Yao, J. Y. Ye, Q. Yuan, F. L. Zhao, Y. F. Li and Z. Y. Zhou, *Adv. Funct. Mater.*, 2021, **31**, 2103671.
- (22) X. T. Yang, Q. Yuan, J. W. Li, T. Sheng, K. X. Yao and X. Wang, *Nano Lett.*, 2023, **23**, 3467-3475.
- (23) A. Marchionni, M. Bevilacqua, C. Bianchini, Y. X. Chen, J. Filippi, P. Fornasiero, A. Lavacchi, H. Miller, L. Wang and F. Vizza, *ChemSusChem*, 2013, **6**, 518-528.
- (24) L. Xin, Z. Y. Zhang, J. Qi, D. Chadderton and W. Z. Li, *Appl. Catal. B*, 2012, **125**, 85-94.
- (25) T. R. Kumar, G. G. Kumar and A. Manthiram, *Adv. Energy Mater.*, 2019, **9**, 1803238.
- (26) Y. Chen, M. Bellini, M. Bevilacqua, P. Fornasiero, A. Lavacchi, H. A. Miller, L. Wang and F. Vizza, *ChemSusChem*, 2015, **8**, 524-533.
- (27) W. Wang, X. Li, Y. S. Cheng, M. Zhang, K. Zhao and Y. H. Liu, *J. Taiwan Inst. Chem. E.*, 2023, **143**, 104714.
- (28) X. Li, J. Deng, X. Deng, Y. Cheng, S. Imhanria and W. Wang, *J. Alloys Compd.*, 2022, **890**, 161899.
- (29) Y. S. Cheng, Y. Sun, X. M. Deng, M. Zhang, L. W. Zhang and W. Wang, *Int. J. Hydrog. Energy*, 2023, **48**, 8156-8164.

(30) K. Matsuoka, Y. Iriyama, T. Abe, M. Matsuoka and Z. Ogumi, *J. Power Sources*, 2005, **150**, 27-31.